Energy Engineering

Tech Science Press

Doi:10.32604/ee.2025.073434

ARTICLE

Sensorless Speed Control of Synchronous Reluctance Motor Using an Advanced Fictitious Flux Estimation Including Cross Coupling Effect

Abdin Abdin[1], Nicola Bianchi[1,*], Andrea Voltan[2], Walter Faedo[2], Piero Cazzavillan[2] and Alessandro Biason[2]

[1]Department of Electrical Engineering, University of Padova, Padova, 35131, Italy
[2]Dana Service and Assembly Center (SAC), Veneto, 35035, Italy

*Corresponding Author: Nicola Bianchi. Email: nicola.bianchi@unipd.it

Received: 18 September 2025; Accepted: 24 December 2025; Published: 27 February 2026

ABSTRACT: Synchronous reluctance motors (SynRM) are widely employed in industrial applications due to their high robustness, low cost, and absence of permanent magnets. In recent years, significant research efforts have focused on improving the controllability and efficiency of SynRM. Accurate rotor position information is essential for the controller to generate appropriate current and voltage references corresponding to the desired speed and load torque. Shaft-mounted position sensors are generally undesirable because of their high cost, sensitivity to harsh operating conditions, maintenance requirements, and reduced reliability in environments characterized by high vibration. Consequently, sensorless control techniques that estimate rotor position using measured stator currents and voltages have attracted increasing attention. However, magnetic saturation, parameter nonlinearities, and cross-coupling effects significantly degrade position estimation accuracy and may compromise the stability of sensorless SynRM drives. In this paper, a nonlinear SynRM model is developed using finite element analysis (FEA) to accurately capture magnetic saturation and cross-coupling effects, thereby providing a precise representation of the machine's electromagnetic behavior under varying load and flux conditions. A series of magnetostatic FEA simulations is performed. To reduce computational complexity, only one motor pole is analyzed by applying anti-periodic boundary conditions along the domain sides and enforcing a zero magnetic vector potential on the external stator boundary. Nonlinear iron material properties are modeled using the appropriate B-H curve. The simulations are carried out by imposing d- and q-axis current components and computing the corresponding flux linkages and electromagnetic torque. Based on these results, both apparent and incremental inductances are extracted and incorporated into the control algorithm. An advanced fictitious flux linkage method combined with a phase-locked loop (PLL) is employed for accurate rotor position estimation. Simulation results confirm that the proposed sensorless control strategy ensures stable operation and high position estimation accuracy over the entire speed range.

KEYWORDS: Sensorless controller 1; advanced active flux 2; fictitious flux 3; magnetic cross-coupling 4; phase locked loop controller 5

1 Introduction

The Synchronous Reluctance Motor (SynRM) has gained considerable attention in industrial applications due to its simple and robust structure, high efficiency, high torque density, and the absence of permanent magnets [1–5]. The independence from rare-earth materials makes SynRMs cost-effective and environmentally sustainable alternatives to conventional AC machines [4]. Furthermore, the absence of rotor windings and permanent magnets results in reduced rotor losses and torque characteristics that are

insensitive to temperature variations [6]. The stator structure is similar to that of an induction motor, featuring three-phase sinusoidally distributed windings supplied by balanced currents [4,7,8], while offering higher torque density and lower manufacturing cost compared to induction motors [9–11].

High-performance SynRM drives require accurate rotor position information to achieve precise speed and torque control [4,12,13]. Although shaft-mounted position sensors can provide this information, their use is often limited by increased cost, reduced reliability in harsh environments, sensitivity to vibration and temperature, and installation constraints [13–16]. Consequently, sensorless control strategies have become increasingly attractive for reliable and low-cost SynRM drive systems.

Recent advances in microcontrollers and power electronics have enabled the development of sensorless SynRM control schemes based on electrical signal measurements [4,17,18]. Among these, model-based position estimation techniques are particularly appealing since they do not require high-frequency voltage injection. However, the strong magnetic saliency of the SynRM rotor introduces significant nonlinearities due to magnetic saturation and cross-coupling, which complicate accurate stator flux and position estimation and may degrade estimator stability [19–21]. Many existing approaches simplify the problem by neglecting these nonlinear effects and relying on voltage-model-based flux estimation [22,23].

The fictitious flux linkage concept, originally proposed in [24,25] and further developed in [26,27], enables rotor position estimation by aligning the fictitious flux with the rotor d-axis. Nevertheless, accurate stator flux estimation remains critical, particularly when magnetic saturation and cross-coupling are present [28]. Recent studies have highlighted the necessity of incorporating nonlinear magnetic effects for reliable sensorless operation [29–31].

In this paper, a nonlinear SynRM model including magnetic saturation and cross-coupling effects is developed using Finite Element Analysis (FEA)-based magnetic mapping. The resulting nonlinear flux linkage lookup tables are integrated into a combined voltage and current model for accurate stator flux estimation. A fictitious flux linkage is then computed and used in conjunction with a Phase-Locked Loop (PLL) to estimate the rotor position. Steady-state and dynamic simulation results validate the effectiveness and robustness of the proposed sensorless control strategy.

2 Modelling of Nonlinear SynRM

To design the controller of the nonlinear SynRM, it is first necessary to develop an accurate nonlinear magnetic model of the machine. This model can be constructed either from measured magnetic characteristics obtained on a test bench or via finite element analysis (FEA) [32–34].

In this section, the nonlinear model of the selected SynRM is developed considering magnetic cross-coupling effects through FEA. To obtain accurate results, a series of magnetostatic FEM analyses is performed following the approach in [35–37]. To enhance computational efficiency while preserving precision, only one pole of the motor is analyzed, with anti-periodic boundary conditions applied on the lateral boundaries and a zero magnetic vector potential enforced on the external stator surface. Nonlinear iron material properties, characterized by the appropriate B–H curve, are adopted. The analyses are conducted by imposing the d- and q-axis current components and computing the corresponding d- and q-axis flux linkages along with the electromagnetic torque.

From the FEA results, and using Eqs. (2), (6), and (7), the stator resistance as well as the apparent and incremental inductances of the motor are determined. These parameters are subsequently used in the controller design and are summarized in Table 1.

Table 1: Motor parameters

Parameter	Symbol	Value	Unit
Nominal voltage	V_N	300	V
Nominal current	I_N	6	A
Stator resistance	R_s	4.6	Ω
Direct axis inductance	L_d	400	mH
Quadrature axis inductance	L_q	54	mH
Number of pole pairs	p	2	–
Nominal torque	τ_N	11.5	Nm
Nominal speed	n_N	1400	rpm
Inertia	J	0.03	kgm^2

The nonlinear equations of the SynRM model are given by

$$\begin{aligned} v_d &= R_s i_d + \frac{d\lambda_d}{dt} - \omega_m^e \lambda_q \\ v_q &= R_s i_q + \frac{d\lambda_q}{dt} + \omega_m^e \lambda_d \end{aligned} \tag{1}$$

Rearranging the above equations yields

$$\begin{aligned} \frac{d\lambda_d}{dt} &= v_d - R_s i_d + \omega_m^e \lambda_q \\ \frac{d\lambda_q}{dt} &= v_q - R_s i_q - \omega_m^e \lambda_d \end{aligned} \tag{2}$$

For the nonlinear SynRM, the flux linkages λ_d and λ_q depend strongly on the operating point (i_d, i_q). The relationships $\lambda_d(i_d, i_q)$ and $\lambda_q(i_d, i_q)$ for the given machine are obtained through FEA.

The flux linkage variations can be expressed as

$$\begin{aligned} d\lambda_d &= \frac{\partial \lambda_d}{\partial i_d} di_d + \frac{\partial \lambda_d}{\partial i_q} di_q \\ d\lambda_q &= \frac{\partial \lambda_q}{\partial i_d} di_d + \frac{\partial \lambda_q}{\partial i_q} di_q \end{aligned} \tag{3}$$

From Eq. (3), the incremental inductances are defined as

$$\begin{bmatrix} l_{dd}(i_d, i_q) & l_{dq}(i_d, i_q) \\ l_{qd}(i_d, i_q) & l_{qq}(i_d, i_q) \end{bmatrix} = \begin{bmatrix} \frac{\partial \lambda_d}{\partial i_d} & \frac{\partial \lambda_d}{\partial i_q} \\ \frac{\partial \lambda_q}{\partial i_d} & \frac{\partial \lambda_q}{\partial i_q} \end{bmatrix} \tag{4}$$

At any operating point (i_d, i_q), the inverse of the incremental inductance matrix defines the inertance matrix:

$$\begin{bmatrix} \gamma_{dd}(i_d, i_q) & \gamma_{dq}(i_d, i_q) \\ \gamma_{qd}(i_d, i_q) & \gamma_{qq}(i_d, i_q) \end{bmatrix} = \begin{bmatrix} l_{dd}(i_d, i_q) & l_{dq}(i_d, i_q) \\ l_{qd}(i_d, i_q) & l_{qq}(i_d, i_q) \end{bmatrix}^{-1} \tag{5}$$

Using Eq. (3), the current variations can then be computed as

$$\begin{aligned} di_d &= \gamma_{dd}(i_d, i_q)d\lambda_d + \gamma_{dq}(i_d, i_q)d\lambda_q \\ di_q &= \gamma_{qd}(i_d, i_q)d\lambda_d + \gamma_{qq}(i_d, i_q)d\lambda_q \end{aligned} \tag{6}$$

Let us remember that the cross incremental inductances I_{dq} and I_{qd} are equal. As a consequence, the inertance γ_{dq} and γ_{qd} are equal

Furthermore, the electromagnetic torque τ_{em} can be calculated from the currents i_d, i_q and flux linkages λ_d, λ_q [38] as:

$$\tau_{em} = \frac{3}{2}p(\lambda_d i_q - \lambda_q i_d) \tag{7}$$

where p is the number of pole pairs.

The nonlinear motor model, shown in Fig. 1, is based on Eqs. (2), (6) and (7).

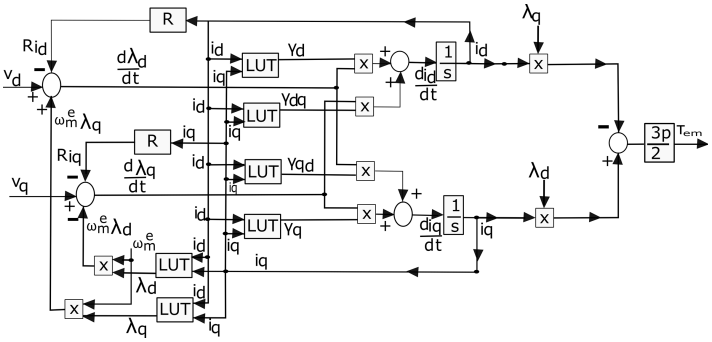

Figure 1: Dynamic motor model

The results obtained from the model shown in Fig. 1 are presented in Fig. 2a,b. These results confirm that a nonlinear model of the SynRM has been successfully developed for control purposes.

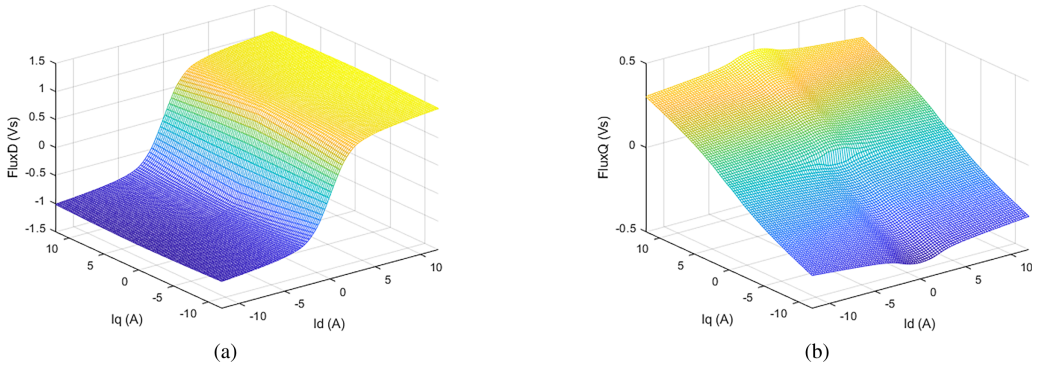

Figure 2: (**a**) Nonlinear d-axis flux λ_d; (**b**) Nonlinear q-axis flux λ_q

2.1 Nonlinear d-Axis Flux Linkage λ_d

Fig. 2a illustrates that the d-axis flux linkage exhibits nonlinear behavior and is influenced by both the direct- and quadrature-axis currents, reflecting the presence of cross-coupling effects.

2.2 Nonlinear q-Axis Flux Linkage λ_q

Fig. 2b illustrates the nonlinear q-axis flux linkage, which is influenced by both the direct- and quadrature-axis currents, including the magnetic cross-coupling effect. It is noteworthy that a significant variation occurs at $i_d \cong 0$, which is attributed to the presence of iron bridges.

3 Design of the Advanced Fictitious Flux Estimator

This section integrates two complementary methods, a voltage integrator and a flux observer, accounting for nonlinear magnetic cross-coupling, to design an advanced fictitious flux linkage estimator. To accurately estimate the rotor position, the fictitious flux linkage is derived from the stable stator flux linkage of the model and processed through a phase-locked loop (PLL) controller for medium- and high-speed operations.

3.1 Voltage Integrator

The voltage equations of the SynRM in the stationary α-β reference frame are

$$\begin{bmatrix} v_\alpha \\ v_\beta \end{bmatrix} = \begin{bmatrix} R_s & 0 \\ 0 & R_s \end{bmatrix} \begin{bmatrix} i_\alpha \\ i_\beta \end{bmatrix} + \frac{d}{dt} \begin{bmatrix} \lambda_\alpha \\ \lambda_\beta \end{bmatrix} \tag{8}$$

where v_α, v_β, i_α, i_β, λ_α, and λ_β are the voltages, currents, and flux linkages in the stationary α-β frame, and R_s is the stator resistance. From Eq. (8), the flux linkage vector $\bar{\lambda}_{\alpha\beta}$ can be computed as

$$\bar{\lambda}_{\alpha\beta} = \int \left(\bar{v}_{\alpha\beta} - R_s \bar{i}_{\alpha\beta} \right) dt \tag{9}$$

At zero or low speed, the back-EMF is negligible, and Eq. (9) fails to provide an accurate estimate of the α-β flux linkages. To overcome this limitation, a flux observer is incorporated into the estimator.

3.2 Flux Observer

To estimate the rotor-frame currents $\hat{i}_{dq}$, the estimated rotor position $\hat{\theta}_m^e$ must be known. The rotor position $\hat{\theta}_m^e$ is obtained using a PLL controller (described below). The current vector $\hat{i}_{dq}$ is computed from the measured α-β currents as

$$\hat{i}_{dq} = \bar{i}_{\alpha\beta} e^{-j\hat{\theta}_m^e} \tag{10}$$

The incremental inductance matrix of the nonlinear magnetic model, obtained from FEA, is given in Eq. (4). The flux linkage vector $\tilde{\lambda}_{dq}$ in the synchronous dq reference frame is then computed as

$$\tilde{\lambda}_{dq} = \begin{bmatrix} l_d & l_{dq} \\ l_{qd} & l_q \end{bmatrix} \begin{bmatrix} \hat{i}_d \\ \hat{i}_q \end{bmatrix} \tag{11}$$

where the tilde denotes that the flux is calculated from the current model. The corresponding flux in the stationary frame is

$$\tilde{\lambda}_{\alpha\beta} = \tilde{\lambda}_{dq} e^{j\hat{\theta}_m^e} \tag{12}$$

Here, $\bar{\lambda}_{\alpha\beta}$ is obtained from the voltage integrator, while $\tilde{\lambda}_{\alpha\beta}$ is obtained from the flux observer. A detailed explanation is provided in Appendix A, including the cross-coupling inductance that causes errors in the

estimation. The flux estimation error is defined as

$$\hat{\lambda}_{error} = \bar{\lambda}_{\alpha\beta} - \tilde{\lambda}_{\alpha\beta} = \bar{\lambda}_{\alpha\beta} - l_{\alpha\beta}\bar{i}_{\alpha\beta} \tag{13}$$

Accurate rotor position estimation requires that $\hat{\lambda}_{error}$ be zero. Since the inductance $l_{\alpha\beta}$ depends on the estimated position $\hat{\theta}_m^e$, $\hat{\lambda}_{error}$ is also a function of $\hat{\theta}_m^e$. The error becomes zero when $\theta_m^e - \hat{\theta}_m^e = 0$. To achieve this, $\hat{\lambda}_{error}$ is transformed into the dq frame using the estimated rotor position, and the resulting dq error is input to a PI controller to drive $\hat{\lambda}_{error}$ to zero. The output of the PI controller provides the estimated stator flux linkage $\hat{\lambda}_{dq}$, which is subsequently transformed back to the stationary frame as $\hat{\lambda}_{\alpha\beta}$, as illustrated in Fig. 3. The estimated flux linkage $\hat{\lambda}_{\alpha\beta}$ is then used to compute the fictitious flux vector, as described in the following subsection.

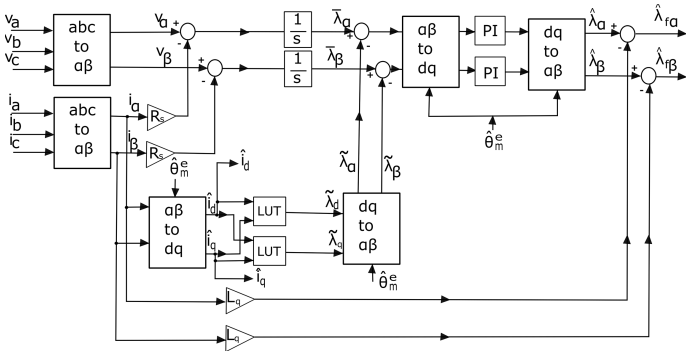

Figure 3: Combined model of the voltage integrator and flux observer for estimating the SynRM stator flux linkage

3.3 Fictitious Flux Linkage Estimation

The flux linkage $\bar{\lambda}_{\alpha\beta}$ in the stationary reference frame is obtained from the measured current $\bar{i}_{\alpha\beta}$ and the applied voltage $\bar{v}_{\alpha\beta}$ as given in Eq. (9). In the synchronous reference frame, the flux linkage is depicted in Fig. 4, and the estimated synchronous frame flux linkage is given by

$$\tilde{\lambda}_{dq} = L_d\hat{i}_d + jL_q\hat{i}_q \tag{14}$$

where the uppercase L denotes the apparent inductances, which are defined at any operating point (i_d, i_q).

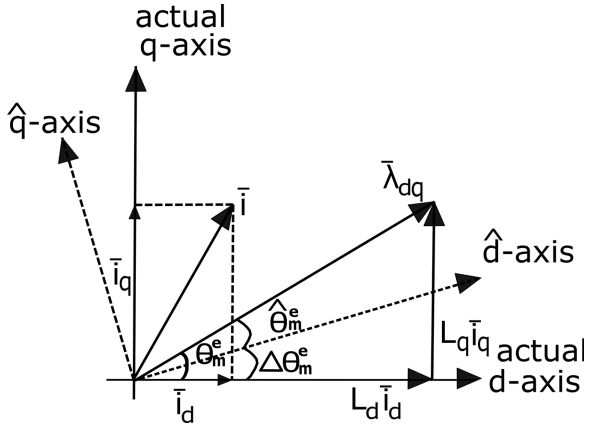

Figure 4: Representation of the synchronous reference frame flux linkage $\boldsymbol{\lambda_{dq}}$

The following remarks are noteworthy:

It is not necessary to estimate the magnitude of the d-axis flux linkage; only its direction needs to be determined. Therefore, any vector aligned with $\hat{\lambda}_d = L_d \hat{i}_d$ can be computed, and its direction provides an indication of the d-axis orientation, as illustrated in Fig. 5.

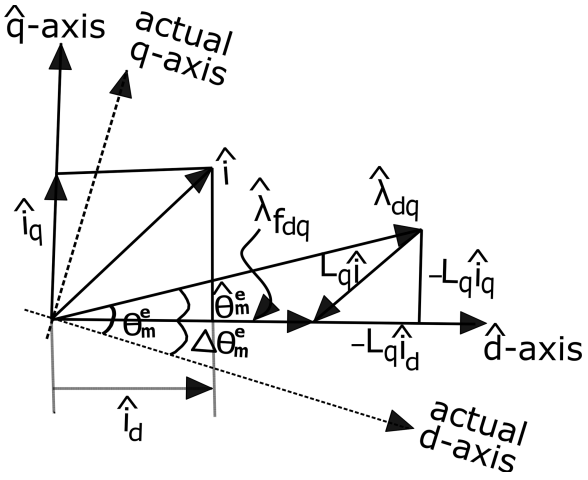

Figure 5: Estimated synchronous reference frame flux linkage $\hat{\lambda}_{dq}$ and fictitious flux linkage

3.4 Determining the Fictitious Flux Linkage Vector $\hat{\lambda}_{f\alpha\beta}$

The fictitious flux linkage vector is defined as

$$\hat{\lambda}_{f\alpha\beta} = \hat{\lambda}_{\alpha\beta} - L_q \hat{i}_{\alpha\beta} \tag{15}$$

Multiplying Eq. (15) by $e^{-j\hat{\theta}^e_m}$ and separating $\hat{\lambda}_{dq}$ and $\hat{i}_{dq}$ into rectangular components yields

$$\hat{\lambda}_{fdq} = (L_d - L_q)\hat{i}_d \tag{16}$$

The estimated electromagnetic torque is then calculated as

$$\hat{\tau}_{em} = \frac{3}{2} p \hat{\lambda}_{fdq} \hat{i}_q \tag{17}$$

The combined model of the voltage integrator and flux observer is shown in Fig. 3.

3.5 Rotor Position Estimation Using a Phase-Locked Loop (PLL) Controller

A PLL controller given in Fig. 6 is employed to estimate the rotor position [39,40].

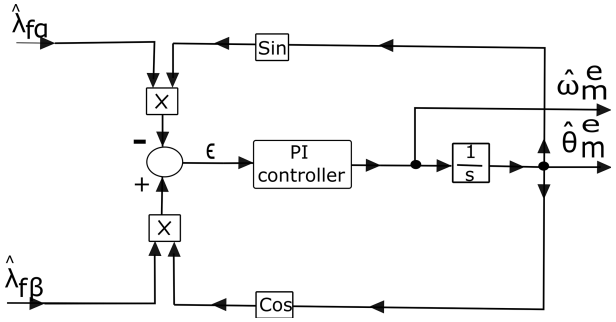

Figure 6: PLL controller for speed and rotor position estimation

Fig. 7 illustrates the vectors $\hat{\theta}_m^e$ and θ_m^e are represented in the plane.

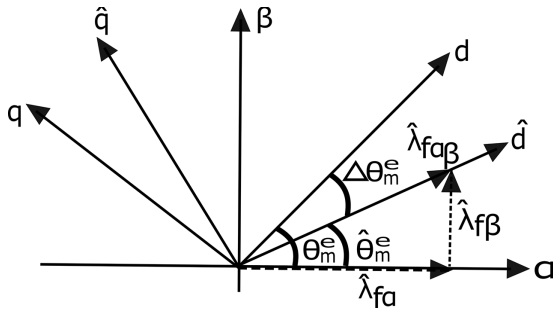

Figure 7: Vector representation of the estimated $\hat{\theta}_m^e$ and actual θ_m^e rotor positions

From Fig. 7, the components of the fictitious flux in the stationary frame are

$$\begin{cases} \hat{\lambda}_{f\alpha} = \hat{\lambda}_f \cos(\theta_m^e) \\ \hat{\lambda}_{f\beta} = \hat{\lambda}_f \sin(\theta_m^e) \end{cases} \tag{18}$$

The position error signal is defined as

$$\epsilon = \hat{\lambda}_{f\beta} \cos(\hat{\theta}_m^e) - \hat{\lambda}_{f\alpha} \sin(\hat{\theta}_m^e) \tag{19}$$

$$= \hat{\lambda}_f \sin(\theta_m^e - \hat{\theta}_m^e) \approx \theta_m^e - \hat{\theta}_m^e \tag{20}$$

From Figs. 6 and 7, it is evident that when $\Delta\theta_m^e = 0$, the estimated values match the actual values. The error signal ϵ serves as the input to a PI controller, whose output provides the estimated rotor speed $\hat{\omega}_m^e$. The estimated rotor position $\hat{\theta}_m^e$ is then obtained by integrating $\hat{\omega}_m^e$.

4 Results and Discussion

The proposed nonlinear model is evaluated using the estimated rotor position $\hat{\theta}_m^e$ and speed $\hat{\omega}_m^e$ obtained from the advanced fictitious flux estimator. The model is simulated with a step reference speed of 146.6 rad/s. At $t = 2$ s, a step load torque equal to the rated torque $\tau_L = 11.5$ Nm is applied. At $t = 4$ s, the

load torque is removed, and the speed is reversed. Finally, at t = 6 s, the rated torque τ_L is applied again. The simulation results demonstrate satisfactory performance under these conditions.

4.1 Stator Flux Linkage Comparison

The accuracy of the proposed estimator depends on both the magnitude and phase of the estimated flux linkage. Deviations in amplitude or phase relative to the actual flux linkage may result in erroneous speed estimation, particularly at high or low speeds. Therefore, the estimator output must remain in phase and match the magnitude of the actual flux linkage under all operating conditions. Fig. 8a–c compares the estimated and actual flux linkages under various operating conditions. It can be observed that the proposed estimator closely tracks the amplitude and phase of the actual flux linkage.

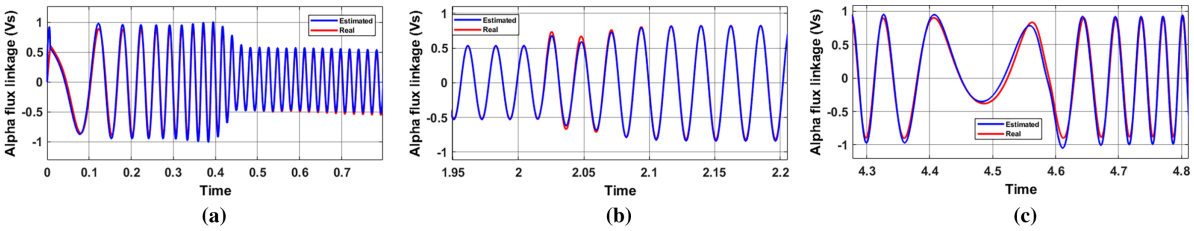

Figure 8: Comparison of estimated and actual stator flux linkage: (**a**) step starting; (**b**) step load torque; (**c**) reversed direction

4.2 Estimated and Actual Speed Comparison

The estimator calculates flux linkage and speed using V_{dq}, I_{dq}, and the L_{dq} inductance lookup table. At standstill, the flux linkage is zero, making speed estimation unreliable. Therefore, the machine is initially started using a rotating current vector based on a fictitious position. Once the speed reaches approximately 20% of the rated speed, the estimator output is used in the speed control loop. Fig. 9a–c shows that while speed estimation is challenging at startup, the estimator accurately tracks the reference speed under step load and correctly estimates reversed speed.

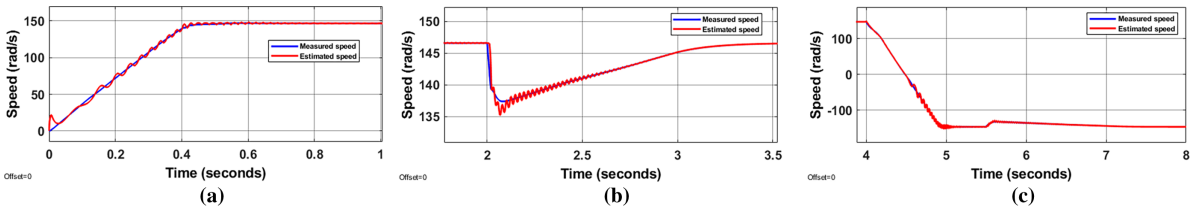

Figure 9: Comparison of estimated and actual rotor speed: (**a**) step starting; (**b**) step load torque; (**c**) reversed direction

4.3 Estimated and Actual Position Comparison

The estimated position is obtained by integrating the estimated speed as shown in Fig. 6. Due to initial speed estimation errors, the position contains an initial offset, as seen in Fig. 10a. Once the speed reaches approximately 20% of the rated value, the estimated position aligns with the actual position within 0.025 s. A minor deviation occurs at the speed reversal, but the estimator rapidly converges to the actual position within 0.26 s (Fig. 10a–c).

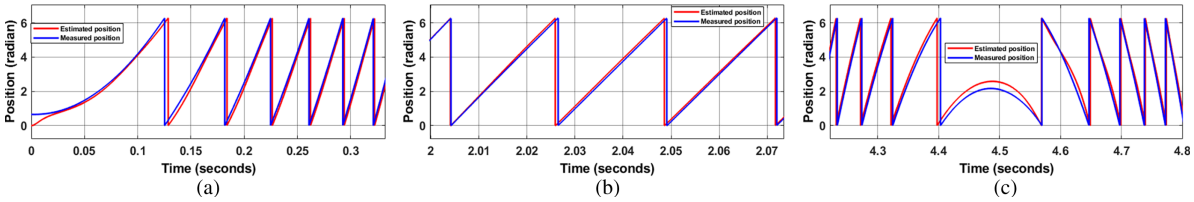

Figure 10: Comparison of estimated and actual rotor position: (**a**) step starting; (**b**) step load torque; (**c**) reversed direction

4.4 Estimated and Actual Electromagnetic Torque Comparison

The actual electromagnetic torque is computed using the nonlinear magnetic model (Eq. 7), while the estimated torque uses the fictitious flux linkage (Eq. 17). Fig. 11a–c demonstrates that the estimator accurately reproduces the electromagnetic torque after a brief transient.

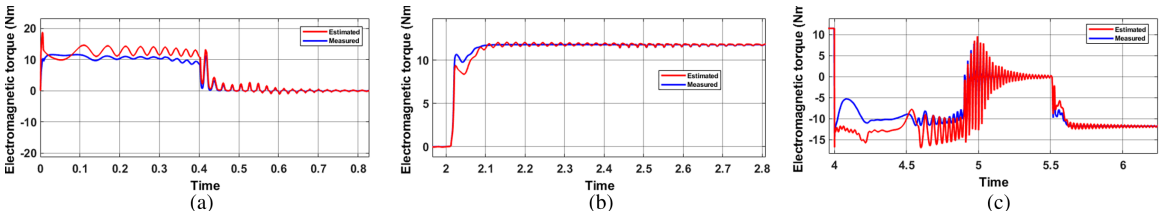

Figure 11: Comparison of estimated and actual electromagnetic torque: (**a**) step starting; (**b**) step load torque; (**c**) reversed direction

4.5 Estimated and Actual Currents I_d and I_q Comparison

Figs. 12 and 13 show the estimated and actual I_d and I_q currents, respectively. The results indicate that the proposed model accurately estimates and controls the I_{dq} currents, meeting the precision requirements of the sensorless current controller.

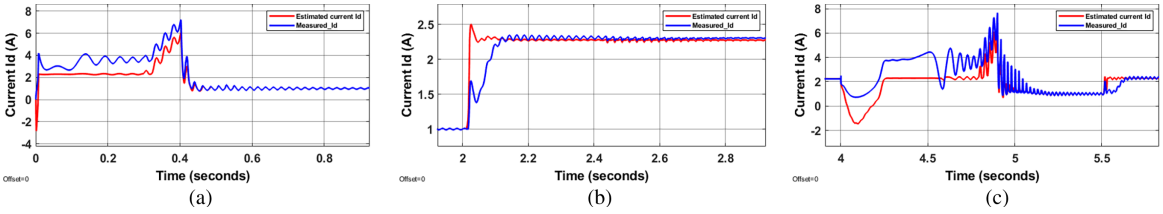

Figure 12: Comparison of estimated and actual I_d current: (**a**) step starting; (**b**) step load torque; (**c**) reversed direction

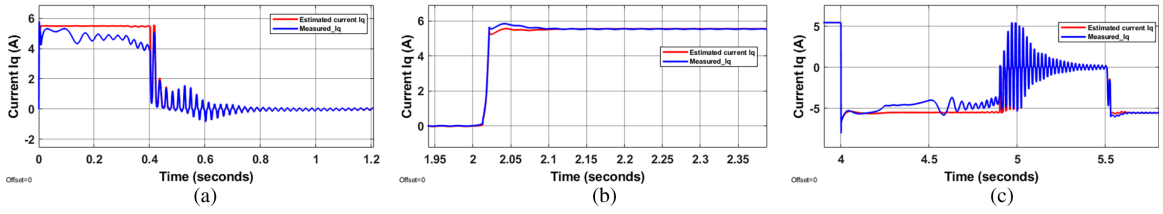

Figure 13: Comparison of estimated and actual I_q current: (**a**) step starting; (**b**) step load torque; (**c**) reversed direction

5 Conclusion

An advanced fictitious flux linkage approach for sensorless operation of SynRM has been presented. The main contributions and novelties of this work are:

1. A nonlinear SynRM model is used, including all effects experienced by a real machine. Unlike most studies that rely on linear dq voltage equations in MATLAB, this model captures saturation and magnetic cross-coupling accurately.
2. Two complementary methodologies, the voltage integrator and flux observer, are combined to estimate the $\alpha\beta$ and dq flux linkages. These estimates are further processed through a fictitious flux estimator in series with a PLL controller, ensuring the estimated speed and position align with the actual values under medium and high-speed conditions.
3. The flux observer employs a lookup table (LUT) of flux linkages across the operating range, allowing precise estimation of instantaneous dq flux linkages from the measured i_{dq} currents.

Simulation results demonstrate that the proposed model is globally stable under all operating conditions without sensors. A nonlinear magnetic model of the SynRM, verified via FEA, is used to account for rotor inductance saturation and cross-coupling effects, issues often neglected in sensorless controller design. The proposed controller overcomes these nonlinearities by using LUTs of flux linkages $\tilde{\lambda}_{\alpha\beta}$ and currents $\hat{i}_{\alpha\beta}$, referenced to the estimated rotor position $\hat{\theta}^e_m$. A PI controller corrects flux linkage errors between the voltage and current models, providing an accurate stator flux linkage. The fictitious flux linkage is aligned with the d-axis current, and the PLL controller accurately estimates rotor position and speed.

Simulation comparisons confirm that the estimated rotor position $\hat{\theta}^e_m$ enables stable sensorless operation of the SynRM. The only limitation is that the machine is not self-starting and requires a rotating current command based on a fictitious position to accelerate to approximately 20% of rated speed for accurate speed and position estimation.

Acknowledgement: We are grateful to DANA for the funding support and all the colleagues in the Electric Drive Laboratory (EDLAB) for their invaluable support in preparation of this article.

Funding Statement: This research was funded by DANA in cordination with Ministerial Decree 117/2023-a.a. 2023/2024–XXXIX Cycle for innovative doctorates that meet the innovation needs of companies.

Author Contributions: The authors confirm contribution to the paper as follows: The conceptualization and methodology is prepared by the project supervisor Nicola Bianchi. Software validation, formal analysis and the investigation are carried by Abdin Abdin and Nicola Bianchi. Data curation and resources are mannaged by Andrea Voltan, Walter Faedo and Abdin Abdin. Original draft is prepared by Piero Cazzavillan, Alessandro Biason and Abdin Abdin. Editing and visualization are done by Piero Cazzavillan and Alessandro Biason. Project adminstrantion and funding acquistion are monitered by Andrea Voltan, Walter Faedo, Piero Cazzavillan and Alessandro Biason. All authors reviewed the results and approved the final version of the manuscript.

Availability of Data and Materials: The data that support the findings of this study are available from the Author, [Abdin Abdin], upon reasonable request.

Ethics Approval: Not applicable. This study did not involve human participants, animal experiments, or data from any individual.

Conflicts of Interest: The authors declare no conflicts of interest to report regarding the present study.

Abbreviations

PLL	Phase locked loop
SynRM	Synchronous reluctance motor
PM	Permanent magnet
FEA	Finite element analysis
PI	Proportional Integral

Appendix A

Eq. (12) can be written in terms of $\bar{i}_{\alpha\beta}$ and $[l_{dq}]$ given as

$$\tilde{\lambda}_{\alpha\beta} = [T]^{-1}[l_{dq}][T]\bar{i}_{\alpha\beta} \tag{A1}$$

where:

$$[T]^{-1} = [T_{dq/\alpha\beta}] = \begin{bmatrix} \cos\hat{\theta}^e_m & \sin\hat{\theta}^e_m \\ -\sin\hat{\theta}^e_m & \cos\hat{\theta}^e_m \end{bmatrix}$$

and

$$[T] = [T_{\alpha\beta/dq}] = \begin{bmatrix} \cos\hat{\theta}^e_m & -\sin\hat{\theta}^e_m \\ \sin\hat{\theta}^e_m & \cos\hat{\theta}^e_m \end{bmatrix}$$

Therefore the following relation can be consider in $\alpha\beta$, as:

$$[l_{\alpha\beta}] = [T]^{-1}[l_{dq}][T] \tag{A2}$$

Joining with (A1) we get

$$\tilde{\lambda}_{\alpha\beta} = [T]^{-1}[l_{dq}][T]\bar{i}_{\alpha\beta} = l_{\alpha\beta}\bar{i}_{\alpha\beta} \tag{A3}$$

Here $l_{\alpha\beta}$ is

$$[l_{\alpha\beta}] = \begin{bmatrix} \cos\hat{\theta}^e_m & \sin\hat{\theta}^e_m \\ -\sin\hat{\theta}^e_m & \cos\hat{\theta}^e_m \end{bmatrix}\begin{bmatrix} l_d & l_{dq} \\ l_{qd} & l_q \end{bmatrix}\begin{bmatrix} \cos\hat{\theta}^e_m & -\sin\hat{\theta}^e_m \\ \sin\hat{\theta}^e_m & \cos\hat{\theta}^e_m \end{bmatrix} \tag{A4}$$

$$= \begin{bmatrix} l_\Sigma - l_\Delta\cos 2\hat{\theta}^e_m - l_\Delta\sin 2\hat{\theta}^e_m & -l_\Delta\sin 2\hat{\theta}^e_m + l_{dq}\cos 2\hat{\theta}^e_m \\ -l_\Delta\sin 2\hat{\theta}^e_m + l_\Delta\cos 2\hat{\theta}^e_m & l_\Sigma + l_\Delta\cos 2\hat{\theta}^e_m + l_{dq}\sin 2\hat{\theta}^e_m \end{bmatrix} \tag{A5}$$

The inductance l_Σ referrs to as the average incremental inductance and it is:

$$l_\Sigma = \frac{l_d + l_q}{2}$$

The inductance l_Δ referred to as the difference incremental inductance and it is:

$$l_\Delta = \frac{l_d - l_q}{2}$$

References

1. Ilioudis VC. A study of MTPA applied to sensorless control of the synchronous reluctance machine (SynRM). Automation. 2025;6(1):11. doi:10.3390/automation6010011.
2. Pellegrino G, Jahns TM, Bianchi N, Soong WL, Cupertino F. The rediscovery of synchronous reluctance and ferrite permanent magnet motors: tutorial course notes. Cham, Switzerland: Springer International Publishing; 2016. doi:10.1007/978-3-319-32202-5.
3. Murataliyev M, Degano M, di Nardo M, Bianchi N, Gerada C. Synchronous reluctance machines: a comprehensive review and technology comparison. Proc IEEE. 2022;110(3):382–99. doi:10.1109/jproc.2022.3145662.
4. Heidari H, Rassõlkin A, Kallaste A, Vaimann T, Andriushchenko E, Belahcen A, et al. A review of synchronous reluctance motor-drive advancements. Sustainability. 2021;13(2):729. doi:10.3390/su13020729.
5. Shilpi, Ramchand R, Lakshmi SLMP. Evolution of multi-phase synchronous reluctance motors: a comprehensive review. J Inform Syst Eng Manag. 2025;10(57s):623–43.
6. Boglietti A, Pastorelli M. Induction and synchronous reluctance motors comparison. In: Proceedings of the 2008 34th Annual Conference of IEEE Industrial Electronics; 2008 Nov 10–13; Orlando, FL, USA. p. 2041–4. doi:10.1109/IECON.2008.4758270..
7. Albassioni KBT, Ibrahim M, El-Kholy EE, Sergeant P. Construction of synchronous reluctance machines with combined star-pentagon configuration using standard three-phase stator frames. IEEE Trans Indust Elect. 2022;69(8):7582–95. doi:10.1109/tie.2021.3105997.
8. Woo TG, Lee SH, Lee HJ, Yoon YD. Flux weakening control technique without look-up tables for SynRMs based on flux saturation models. Electronics. 2020;9(2):218. doi:10.3390/electronics9020218.
9. Boazzo B, Vagati A, Pellegrino G, Armando E, Guglielmi P. Multipolar ferrite-assisted synchronous reluctance machines: a general design approach. IEEE Trans Indust Elect. 2015;62(2):832–45. doi:10.1109/tie.2014.2349880.
10. Capolino GA, Cavagnino A. New trends in electrical machines technology—Part I. IEEE Trans Indust Elect. 2014;61(8):4281–5. doi:10.1109/tie.2013.2295770.
11. Vagati A. The synchronous reluctance solution: a new alternative in AC drives. In: Proceedings of the IECON'94—20th Annual Conference of IEEE Industrial Electronics; 1994 Sep 5–9; Bologna, Italy. p. 1–13. doi:10.1109/IECON.1994.397741.
12. Accetta A. Robust control of synchronous reluctance motor based on automatic disturbance rejection. IEEE Open J Ind Applicat. 2024;5:209–23. doi:10.1109/ojia.2024.3399009.
13. Boztas G, Aydogmus O. Implementation of sensorless speed control of synchronous reluctance motor using extended Kalman filter. Eng Sci Technol Int J. 2022;31:101066. doi:10.1016/j.jestch.2021.09.012.
14. Habyarimana M, Adebiyi AA. Selection and placement of sensors for electric motors: a review and preliminary investigation. Energies. 2025;18(13):3484. doi:10.3390/en18133484.
15. Ran Y, Qiao M, Sun L, Xia Y. Review of position sensorless control technology for permanent magnet synchronous motors. Energies. 2025;18(9):2302. doi:10.3390/en18092302.
16. Tuovinen T, Hinkkanen M, Harnefors L, Luomi J. A reduced-order position observer with stator-resistance adaptation for synchronous reluctance motor drives. In: Proceedings of the 14th International Power Electronics and Motion Control Conference EPE-PEMC 2010; 2010 Sep 6–8; Ohrid, Macedonia. p. T5-174T5179. doi:10.1109/EPEPEMC.2010.5606645.
17. Cai H, Luo W. Full-speed sensorless control system of synchronous reluctance motor with flux saturation model. Sci Rep. 2025;15(1):9048. doi:10.1038/s41598-025-92441-7.
18. Nikmaram B, Mousavi MS, Khalaji Z, Davari SA, Rodriguez J, Fazeli M. Sensorless control of synchronous reluctance motors based on newton-raphson iteration algorithm. In: Proceedings of the 2023 3rd International Conference on Electrical Machines and Drives (ICEMD); 2023 Dec 20–21; Tehran, Iran. p. 1–6. doi:10.1109/ICEMD60816.2023.10429587.
19. Farhan A, Abdelrahem M, Hackl CM, Kennel R, Shaltout A, Saleh A. Advanced strategy of speed predictive control for nonlinear synchronous reluctance motors. Machines. 2020;8(3):44. doi:10.3390/machines8030044.
20. Hackl CM. Non-identifier based adaptive control in mechatronics: theory and Application. Vol. 466. Cham, Switzerland: Springer; 2017. doi:10.1007/978-3-319-55036-7.

21. Hackl CM, Kamper MJ, Kullick J, Mitchell J. Nonlinear PI current control of reluctance synchronous machines. arXiv:1512.09301. 2015. doi:10.48550/arXiv.1512.09301.
22. Lagerquist R, Boldea I, Miller TJE. Sensorless-control of the synchronous reluctance motor. IEEE Trans Indust Applicat. 1994;30(3):673–82. doi:10.1109/28.293716.
23. Capecchi E, Guglielmi P, Pastorelli M, Vagati A. Position sensorless control of transverse-laminated synchronous reluctance motors. In: Proceedings of the Conference Record of the 2000 IEEE Industry Applications Conference. Thirty-Fifth IAS Annual Meeting and World Conference on Industrial Applications of Electrical Energy (Cat. No.00CH37129); 2000 Oct 8–12; Rome, Italy. p. 1766–73. doi:10.1109/IAS.2000.882119.
24. Koonlaboon S, Sangwongwanich S. Sensorless control of interior permanent-magnet synchronous motors based on a fictitious permanent-magnet flux model. In: Proceedings of the Fourtieth IAS Annual Meeting. Conference Record of the 2005 Industry Applications Conference; 2005 Oct 2–6; Hong Kong, China. p. 311–8. doi:10.1109/IAS.2005.1518326.
25. Sangwongwanich S, Suwankawin S, Po-ngam S, Koonlaboon S. A unified speed estimation design framework for sensorless AC motor drives based on positive-real property. In: Proceedings of the 2007 Power Conversion Conference–Nagoya; 2007 Apr 2–5; Nagoya, Japan. p. 1111–8. doi:10.1109/PCCON.2007.373105.
26. Boldea I, Paicu MC, Andreescu GD. Active flux concept for motion-sensorless unified AC drives. IEEE Trans Power Elect. 2008;23(5):2612–8. doi:10.1109/tpel.2008.2002394.
27. Boldea I, Andreescu GD, Rossi C, Pilati A, Casadei D. Active flux based motion-sensorless vector control of DC-excited synchronous machines. In: Proceedings of the 2009 IEEE Energy Conversion Congress and Exposition; 2009 Sep 20–24; San Jose, CA, USA. p. 2496–503. doi:10.1109/ECCE.2009.5316509.
28. Accetta A, Cirrincione M, Pucci M, Sferlazza A. Space-vector state dynamic model of the SynRM considering self, cross-saturation and iron losses and related identification technique. IEEE Trans Indust Applicat. 2023;59(3):3320–31. doi:10.1109/tia.2023.3252528.
29. Pinyopawasutti T, Sangwongwanich S. Fictitious flux and a globally stable observer for sensorless control of synchronous reluctance motors. In: Proceedings of the 2018 International Electrical Engineering Congress (iEECON); 2018 Mar 7–9; Krabi, Thailand. p. 1–4. doi:10.1109/IEECON.2018.8712167.
30. Berto M, Alberti L, Manzolini V, Bolognani S. Computation of self-sensing capabilities of synchronous machines for rotating high frequency voltage injection sensorless control. IEEE Trans Indust Elect. 2022;69(4):3324–33. doi:10.1109/tie.2021.3071710.
31. Drobnič K, Gašparin L, Fišer R. Fast and accurate model of interior permanent-magnet machine for dynamic characterization. Energies. 2019;12(5):783. doi:10.3390/en12050783.
32. Łyskawinski W, Jędryczka C, Stachowiak D, Łukaszewicz P, Czarnecki M. Finite element analysis and experimental verification of high reliability synchronous reluctance machine. Eksploat I Niezawodn. 2022;24(2):386–93. doi:10.17531/ein.2022.2.20.
33. Li C, Wang G, Zhang G, Zhao N, Xu D. Review of parameter identification and sensorless control methods for synchronous reluctance machines. Chinese J Elect Eng. 2020;6(2):7–18. doi:10.23919/cjee.2020.000007.
34. Varvolik V, Prystupa D, Buticchi G, Peresada S, Galea M, Bozhko S. Co-simulation analysis for performance prediction of synchronous reluctance drives. Electronics. 2021;10(17):2154. doi:10.3390/electronics10172154.
35. Nardo MD, Calzo GL, Galea M, Gerada C. Design optimization of a high-speed synchronous reluctance machine. IEEE Trans Indust Applicat. 2018;54(1):233–43. doi:10.1109/tia.2017.2758759.
36. Sizov GY, Zhang P, Ionel DM, Demerdash NAO, Rosu M. Automated bi-objective design optimization of multi-MW direct-drive PM machines using CE-FEA and differential evolution. In: Proceedings of the 2011 IEEE Energy Conversion Congress and Exposition; 2011 Sep 17–22; Phoenix, AZ, USA. p. 3672–8. doi:10.1109/ECCE.2011.6064267.
37. Lee D, Kim JW, Lee CG, Jung SY. Variable mesh adaptive direct search algorithm applied for optimal design of electric machines based on FEA. IEEE Trans Magnetics. 2011;47(10):3232–5. doi:10.1109/tmag.2011.2152380.
38. Khude JT, Shaikh AH, Ugale R. Comparative analysis of 5 HP SynRM And FeA-SynRM for EV applications. In: Proceedings of the 2024 International Conference on Vehicular Technology and Transportation Systems (ICVTTS); 2024 Sep 27–28; Bangalore, India. p. 1–6. doi:10.1109/ICVTTS62812.2024.10763949.

39. Xu A, Li X, Hu S, Liu X. Sensorless control of permanent magnet-assisted synchronous reluctance motor based on adaptive sliding mode observer. Progress Electromag Res Letters. 2024;117:33–40. doi:10.2528/PIERL23103001.
40. Murr M, Giaouris D. Universal PLL strategy for sensorless speed and position estimation of AC motor drives. IEEE Trans Indust Elect. 2009;56(8):2894–904. doi:10.1109/iciinfs.2008.4798473.